Spatially localized states in Marangoni convection in binary mixtures

Pauline Assemat, Alain Bergeon, Edgar Knobloch

Spatially localized states in Marangoni convection in binary mixtures☆

P. Assemat[a,*], A. Bergeon[a], E. Knobloch[b]

[a] *IMFT UMR CNRS 5502-UPS UFR MIG, 31062 Toulouse Cedex, France*
[b] *Department of Physics, University of California, Berkeley, CA 94720, USA*

Abstract

Two-dimensional Marangoni convection in binary mixtures is studied in periodic domains with large spatial period in the horizontal. For negative Soret coefficients convection may set in via growing oscillations which evolve into standing waves. With increasing amplitude these waves undergo a transition to traveling waves, and then to more complex waveforms. Out of this state emerge stable stationary spatially localized structures embedded in a background of small amplitude standing waves. The relation of these states to the time-independent spatially localized states that characterize the so-called pinning region is investigated by exploring the stability properties of the latter, and the associated instabilities are studied using direct numerical simulation in time.

Keywords: Marangoni convection; Spatially localized states; Homoclinic snaking

1. Introduction

Surface tension-driven flows are of importance in a variety of applications, and are a consequence of surface tension inhomogeneities that are either imposed externally or develop spontaneously as a result of an instability. Typical of these is the Marangoni instability that sets in in liquids with a temperature-dependent surface tension once the temperature difference, measured by the Marangoni number, exceeds

* Corresponding author.
E-mail address: assemat@imft.fr (P. Assemat).

a critical value. Such flows occur even in the absence of gravity. In binary mixtures in which the surface tension depends in addition on concentration, temperature-induced concentration inhomogeneities can either enhance instability or lead to overstability, depending on the sign of the Soret coefficient (Castillo and Velarde, 1978, 1982; Bergeon et al., 1994, 1995, 1998; Bergeon and Knobloch, 2004). In the latter case the resulting overstable convection may coexist with steady overturning convection that sets in at a larger value of the Marangoni number. Typically the overstable oscillations are supercritical, while steady convection is subcritical.

In the present paper we are interested in exploring the resulting region of bistability in greater detail. Recent work on two related systems, binary fluid convection (Batiste et al., 2006) and natural doubly diffusive convection (Bergeon and Knobloch, 2007) showed that in this regime time-independent *spatially localized* convection may be present, and uncovered an unexpectedly rich multiplicity of such states. Following Blanchflower (1999) we call these states *convectons*. This behavior has been attributed to the presence of so-called homoclinic snaking in these systems, a phenomenon that is well understood in spatially reversible fourth order systems on the real line with variational structure (Champneys, 1998; Burke and Knobloch, 2006). In particular, in binary mixture convection the convectons emerge from a state called dispersive chaos as the Rayleigh number is increased via a remarkable sequence of relaxation oscillations (Batiste et al., 2006; Alonso et al., 2007). These states are stable despite being embedded within an unstable state, the conduction state, something that is possible when the conduction state is convectively but not absolutely unstable (Batiste et al., 2006). In contrast, above the snaking region the fronts bounding the localized states unpin, and the convecting state grows at the expense of the conduction state, until the whole domain is filled with convection cells.

The system studied here differs from both binary fluid convection and natural doubly diffusive convection, although like the others it is reversible in space and nonvariational. Specifically, the time-independent binary fluid system studied in Batiste et al. (2006) and Alonso et al. (2007) is equivariant under the spatial reflection $R : x \to -x$, where x is the horizontal coordinate, and hence is reversible as a dynamical system in space, i.e., with x playing the role of a time-like variable. In this case R acts on the fields by $+1$ (see below). However, the system is in addition also equivariant under a second reflection, the reflection κ in the layer midplane. This symmetry is present as a consequence of the Boussinesq approximation and the use of identical boundary conditions at the top and bottom of the layer, and is responsible for the presence in this system of convectons of both even and odd parity. The even convectons, that is, states that are invariant under $R_\ell : x \to \ell - x$ for a suitably chosen ℓ, are expected to be time-independent solutions of R-equivariant systems. This is not so of the odd parity convectons. In generic R-equivariant systems such states are expected to drift in the x-direction, but here their drift is prevented by the symmetry κR_ℓ of these states. Thus the binary convection example exhibits two classes of steady localized states, of opposite parity with respect to R. Since each state can also be reflected in the layer midplane there are in fact four branches of localized states each of which undergoes homoclinic snaking in the same region of parameter space.

In contrast, the natural doubly diffusive system studied in Bergeon and Knobloch (2007) possesses only the symmetry $\Delta \equiv \kappa R$ but the symmetry R is absent. Moreover, the symmetry Δ acts on the fields by -1. As a result there are only two branches of steady convectons, and both are invariant under $\Delta_\ell \equiv \kappa R_\ell$ for suitable ℓ.

The Marangoni convection problem studied here shares many properties with the binary convection system but lacks the additional symmetry κ. As a result we expect only two types of time-independent convectons, both even with respect to R_ℓ, but distinguished by the direction of the flow along the line of

symmetry, $x = \Gamma/2$, where Γ is the dimensionless length of the periodic domain. All odd parity states now drift, and must be located by solving an appropriate nonlinear eigenvalue problem for the drifting localized states and their drift speed. Moreover, for the parameter values used here the time-independent even parity convectons emerge with increasing Marangoni number from a time-dependent state consisting of a spatially localized structure embedded in a background of small amplitude standing waves.

The paper is organized as follows. In Section 2 we introduce the basic equations of the study, and review the numerical techniques used to compute the solutions. These include numerical branch following techniques as well as direct numerical simulation. Our results are presented in Section 3, and interpreted theoretically in Section 4.

2. Marangoni convection

2.1. Equations and dimensionless parameters

We study two-dimensional Marangoni convection in the presence of a Soret effect in a spatially periodic domain of period $\Gamma = n\lambda_c$, where n is an integer and $\lambda_c \approx 3.1$ is the critical wavelength for the onset of convection in a single component liquid. A constant normal heat flux $-q > 0$ is applied (in the downward direction) at the free upper surface. The velocity vanishes along the bottom wall, assumed to be no-slip. The surface tension σ along the free upper surface varies linearly with the surface temperature and concentration: $\sigma = \sigma_0(1 + \gamma_T T + \gamma_C C)$, where σ_0 is a constant. We assume that to leading order the free surface remains undeformed by the flow (σ is large) and assume that the gas in contact with the free surface has no influence.

In the following distance, time, temperature, concentration and velocity are nondimensionalized using H, H^2/ν, $\Delta T \equiv -qH/\lambda$, $\Delta C \equiv -D_S \Delta T/D$ and $Ma\nu/H$, respectively. Here $Ma \equiv -qH^2\sigma_0\gamma_T/\lambda\rho\nu\kappa_T$ is the flux Marangoni number, and ρ is the density of the fluid, ν is its kinematic viscosity, κ_T is its thermal diffusivity, and $\lambda \equiv C_V \rho\kappa_T$ is the thermal conductivity. In addition D is the concentration diffusivity and D_S is the Soret diffusion coefficient. In zero gravity the system is described by the dimensionless equations (Bergeon and Knobloch, 2004):

$$\partial_t \mathbf{u} = -Ma(\mathbf{u}\cdot\nabla)\mathbf{u} - \nabla p + \nabla^2\mathbf{u}, \quad \nabla\cdot\mathbf{u} = 0, \tag{1}$$

$$\partial_t T = -Ma(\mathbf{u}\cdot\nabla)T + Pr^{-1}\nabla^2 T, \tag{2}$$

$$\partial_t C = -Ma(\mathbf{u}\cdot\nabla)C + Sc^{-1}(\nabla^2 C - \nabla^2 T), \tag{3}$$

where $\mathbf{u}$, p, T, C are, respectively, the dimensionless velocity, pressure, temperature and concentration, and $Pr \equiv \nu/\kappa_T$ and $Sc \equiv \nu/D$ are the Prandtl and Schmidt numbers. The boundary conditions along the free surface ($z = 1$) are

$$\partial_z u - Pr^{-1}(\partial_x T + S_M \partial_x C) = w = \partial_z T - 1 = \partial_z(C - T) = 0, \tag{4}$$

while those along the bottom ($z = 0$) are

$$u = w = T = \partial_z(C - T) = 0. \tag{5}$$

Here

$$S_M = -\frac{D_S\gamma_C}{D\gamma_T}$$

is a dimensionless quantity analogous to the separation ratio familiar from buoyancy-driven convection. In the following we shall be interested in mixtures with $S_M < 0$. In this case the conduction case may lose stability with increasing Marangoni number to growing oscillations; the physical mechanism of this instability is discussed in Bergeon and Knobloch (2004). Note that for liquids with $\gamma_T < 0$ we must reverse the sign of q, i.e., the surface must be cooled to generate instability instead of being heated.

The above problem has the solution $\mathbf{u}=\mathbf{0}$, $T_0(z)=z$, $C_0(z)=z$, present for all values of Ma, corresponding to the conduction state. In the following we study the states resulting from instability of this state in periodic domains with moderately large spatial period Γ. As already explained, in the present case the R-symmetry acts by $+1$, and hence R-symmetric states satisfying

$$u(-x,z)=-u(x,z), \quad w(-x,z)=w(x,z), \quad T(-x,z)=T(x,z), \quad C(-x,z)=C(x,z) \tag{6}$$

play a prominent role.

2.2. *Numerical method*

To solve the above equations we use a numerical continuation method based on a Newton solver for the time-independent version of Eqs. (1)–(3) with the boundary conditions (4)–(5). The implementation of the method follows that of Tuckerman (1989) and Mamun and Tuckerman (1995), but employs a spectral element method in which the domain $[0,1]\times[0,\Gamma]$ is decomposed into N_e macro-elements of size $[0,1]\times[i\Gamma/N_e,(i+1)\Gamma/N_e]$, where N_e is the number of spectral elements and $i \in \{0,\ldots,N_e-1\}$. In each element, the fields are approximated by a high order interpolant through the Gauss–Lobatto–Legendre points (Funaro, 1991). The Newton solver uses a first order time-stepping scheme for the equations in conservation form; we use the scheme proposed by Karniadakis et al. (1991) in which the diffusive linear part of the equations is treated implicitly. Each time step therefore requires the inversion of four Helmholtz problems. This is carried out using a Schur factorization procedure on the weak form of the equations (Deville et al., 2002), a procedure that ensures the periodicity of the unknowns and their first derivative in the x-direction. The dynamical behavior in time is computed using a second order version of the scheme (Karniadakis et al., 1991).

Two types of states are of interest: spatially periodic wavetrains and spatially *localized* states. In domains of finite spatial period Γ only the former bifurcate from the conduction state; the latter bifurcate in secondary pitchfork bifurcations from the periodic states, and do so already at small amplitude when Γ is large. All results are computed for $Sc = 50$, $Pr = 1$ with $\Gamma = 6\lambda_c$ or $\Gamma = 10\lambda_c$, where $\lambda_c \approx 3.1$ is the wavelength of the primary unstable mode.

3. Results

We focus on two representative values of the separation ratio S_M, $S_M = -0.002$ and $S_M = -0.005$. We present the results in the form of bifurcation diagrams showing either the velocity norm $E \equiv \int_0^1 \int_0^\Gamma (u^2 + w^2)\,\mathrm{d}x\,\mathrm{d}z$ or $\Delta T_m \equiv \max|T(x,z) - T_0(z)|$ as functions of Ma. Stability of each branch is indicated using the notation $n - p$, where n is the number of unstable real eigenvalues, and p is the number of *pairs* of unstable complex eigenvalues. Thus the number of unstable eigenvalues is $n + 2p$. In the figures we use solid (dashed) lines to indicate solutions that are stable (unstable) with respect to R-symmetric perturbations of period Γ, and use solid circles, open circles and solid squares to indicate the location of

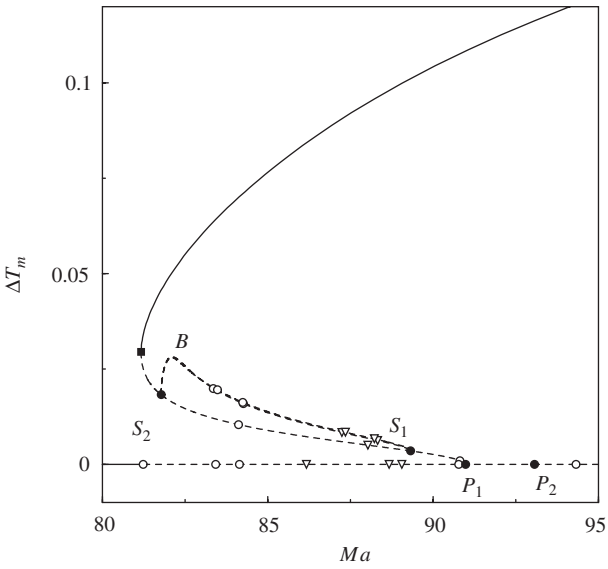

Fig. 1. Bifurcation diagram showing $\Delta T_m \equiv \max |T(x, z) - T_0(z)|$ as a function of the Marangoni number Ma. The two branches labeled B between $M_{a_{S1}} = 89.33$ and $M_{a_{S2}} = 81.78$ are almost identical but are not related by symmetry. Parameters are $Sc = 50$, $Pr = 1$, $S_M = -0.002$ and $\Gamma = 6\lambda_c$. Resolution is $N_e = 12$ with $N_x = 11$ and $N_z = 17$.

pitchfork, Hopf and saddle-node bifurcations; open triangles indicate collisions of complex eigenvalues on the real axis and hence do not correspond to a change in stability. Stability with respect to R-symmetry breaking perturbations is discussed in the text as necessary. With the exception of the primary branch of traveling waves we do not follow branches of time-periodic states. The steady states are all computed by imposing the reflection symmetry $R_{\Gamma/2}$, i.e., reflection symmetry with respect to the line $x = \Gamma/2$.

3.1. The case $S_M = -0.002$, $\Gamma = 6\lambda_c$

We show the results for $S_M = -0.002$, $\Gamma = 6\lambda_c$ in Fig. 1. The figure shows that for these parameter values the conduction state loses stability at $Ma \approx 81.24$ to exponentially growing oscillations with wavenumber $n = 6$, followed by two additional Hopf bifurcations; with increasing Marangoni number the corresponding eigenvalues collide pairwise on the positive real axis and thereafter remain real. The first of these eigenvalues crosses into the negative half plane at $Ma \approx 90.99$ resulting in a pitchfork of revolution to a spatially periodic steady state with wavenumber $n = 6$ (Fig. 2). A second pitchfork of revolution, to states with $n = 7$, follows at $Ma \approx 93.08$. The first of the Hopf bifurcations is supercritical and evolves into a stable standing wave. In contrast, the first pitchfork of revolution is subcritical and the resulting steady spatially periodic states are therefore initially five times unstable (Fig. 3). These undergo a secondary pitchfork bifurcation (S_1) to a spatially modulated state, followed by a secondary Hopf bifurcation before undergoing a further pitchfork (S_2), after which the periodic solutions are only once unstable; these states acquire stability at a saddle-node bifurcation at $Ma \approx 81.175$, and are thereafter stable.

In Fig. 4 we show sample solutions along one of the branches B created at S_1 and destroyed at S_2. The figure reveals a tendency towards modulation with a spatial scale comparable to the imposed period, and suggests a tendency towards spatial localization. The states shown are correctly described as an $n = 1$

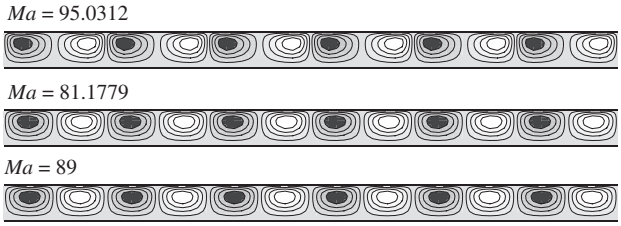

Fig. 2. Solution streamlines at several locations along the P_1 branch; white regions correspond to clockwise flow while black regions correspond to counter-clockwise flow. Contour density does not reflect absolute strength of flow. The Marangoni number $Ma = 89.0$ ($E = 0.23 \times 10^{-05}$) is close to P_1, $Ma = 81.1779$ ($E = 0.15 \times 10^{-03}$) is close to the saddle-node, and $Ma = 95.0312$ ($E = 0.24 \times 10^{-02}$) is along the stable part of the branch. Parameters are $Sc = 50$, $Pr = 1$, $S_M = -0.002$ and $\Gamma = 6\lambda_c$. Resolution is $N_e = 12$ with $N_x = 11$ and $N_z = 17$.

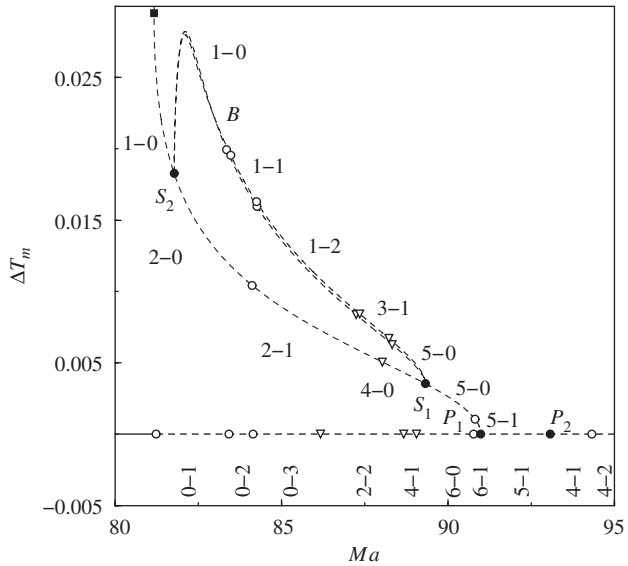

Fig. 3. Enlargement of Fig. 1 indicating the stability properties of the different solution branches. Stability is indicated using the notation $n - p$, where n is the number of unstable real eigenvalues, and p is the number of *pairs* of unstable complex eigenvalues. Thus none of nontrivial solutions is stable. Parameters are $Sc = 50$, $Pr = 1$, $S_M = -0.002$ and $\Gamma = 6\lambda_c$. Resolution is $N_e = 12$ with $N_x = 11$ and $N_z = 17$.

modulation of a finite amplitude $n = 6$ state. Each has a line of symmetry at $x = \Gamma/2$, corresponding to a region of upflow. Solutions with downflow at $x = \Gamma/2$ are also present, but differ in detail: there is no symmetry that takes an upflow state into a downflow state. Despite this the bifurcations at S_1 and S_2 are pitchforks. This is a consequence of the fact that the 1:6 spatial resonance is a *weak* spatial resonance (Prat et al., 1998). Although both the upflow and the downflow states undergo two tertiary Hopf bifurcations each of which decreases their degree of instability, neither ever acquires stability.

We have not explored the branches created in the various bifurcations described above but observe that the scenario described resembles that identified in doubly diffusive convection in a horizontal layer

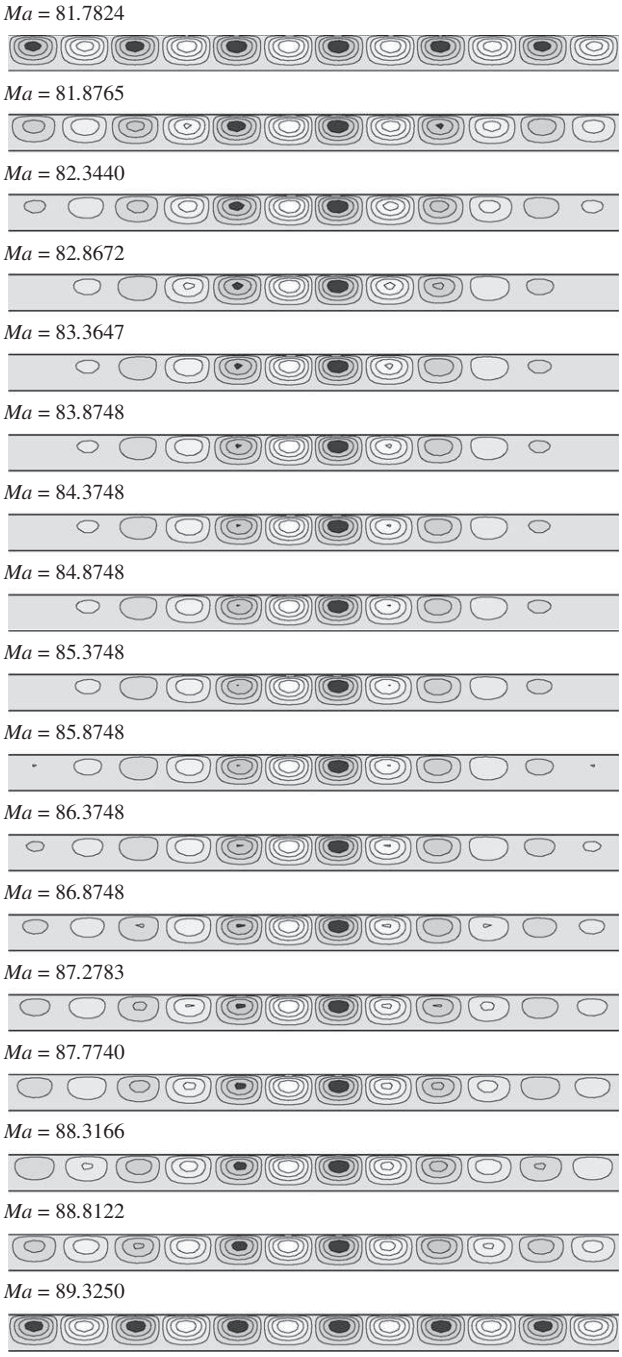

Fig. 4. Solution streamlines at different locations along one of the branches B bifurcating subcritically at S_1 from the first primary periodic branch. The values of Ma decrease from bottom (close to S_1) to top (close to S_2). Parameters are $Sc = 50$, $Pr = 1$, $S_M = -0.002$ and $\Gamma = 6\lambda_c$. Resolution is $N_e = 12$ with $N_x = 11$ and $N_z = 17$.

(Moore and Weiss, 2000) in a smaller domain (and in the presence of the additional reflection symmetry κ). In the following we use the observed behavior as motivation for looking for time-independent spatially localized states. For this purpose it is advantageous to examine the regime in which the primary steady state branch is more subcritical, i.e., a smaller value of S_M, and to examine the solutions in a larger domain.

3.2. The case $S_M = -0.005$, $\Gamma = 10\lambda_c$

3.2.1. Time-independent states

Figs. 5a–c show the results for $S_M = -0.005$, $\Gamma = 10\lambda_c$. This time the figures show the velocity norm E as a function of Ma, focusing on branches of steady states only. The figures show two primary branches of spatially periodic states, labeled P_1 and P_2, that bifurcate from the conduction state in close succession, with P_1 preceding P_2. Of these P_1 corresponds to states with 11 wavelengths ($n = 11$) within the imposed spatial period, while P_2 corresponds to 10 wavelengths ($n = 10$). Both branches bifurcate strongly subcritically. Fig. 5c shows that P_1 undergoes a secondary pitchfork bifurcation already at very small amplitude, producing a pair of states labeled L_1, L_2, followed at larger amplitude by two further pitchfork bifurcations, the second of which produces the branches labeled B_1; the P_2 branch likewise undergoes a secondary bifurcation to a pair of branches labeled B_2. The two states L_1, L_2 created in the first of these bifurcations both have spatial wavenumber $n = 11$, modulated by wavenumber $n = 1$, but once again are not related by symmetry. As a result the two branches of localized states in Fig. 5c differentiate with decreasing Ma into distinct branches (Fig. 5a); as this occurs the modulation amplitude increases and the emerging states become more and more spatially localized. Near $Ma \approx 83.4$ the two branches undergo a sequence of saddle-node bifurcations as both branches begin to oscillate back and forth, in a behavior known as *snaking*. In this region the localized states grow in extent, each type adding a roll on each side as one proceeds up the snaking branch in such a way that the symmetry R of the state is preserved. When the localized states almost fill the domain Γ the snaking ends and both branches turn over to connect to a primary branch of periodic states. In the present case both terminate on the branch P_2, once again in a pitchfork bifurcation. Thus the two snaking branches provide a connection between the two primary branches P_1 and P_2.

Fig. 6 shows the evolution of the localized states as one proceeds from the secondary pitchfork on the P_1 branch to the secondary pitchfork on the P_2 branch. All states shown are R-symmetric; the states numbered (1)–(6) have minimum amplitude in the center of the domain and lie on the branch labeled L_1, while those numbered (7)–(10) lie on L_2 and have maximum amplitude in the center. After translation by $\Gamma/2$ the L_1 states, like the L_2 states, are localized in the center of the periodic domain, with L_1 (L_2) characterized by an upflow (downflow) at $x = \Gamma/2$. Once again these two states are unrelated by any symmetry.

Near P_1 both L_1 and L_2 have 11 wavelengths and are weakly modulated over the period Γ; the upflow state L_1 bifurcates from the P_1 state with upflow at $x = \Gamma/2$, while the downflow state L_2 bifurcates from the half-wavelength translate of this P_1 state, with downflow at $x = \Gamma/2$. As Ma decreases both patterns contract, eventually forming states consisting of a few dominant pairs of rolls, with the rest of the domain filled with the conduction state. At this point both branches start to snake, and the localized states begin to spread laterally by nucleating rolls pairwise on either side. Once the domain is almost full the solutions resemble holes in an otherwise periodic state, with the hole becoming shallower and wider as one approaches the termination of the branch. At this point the solutions therefore resemble

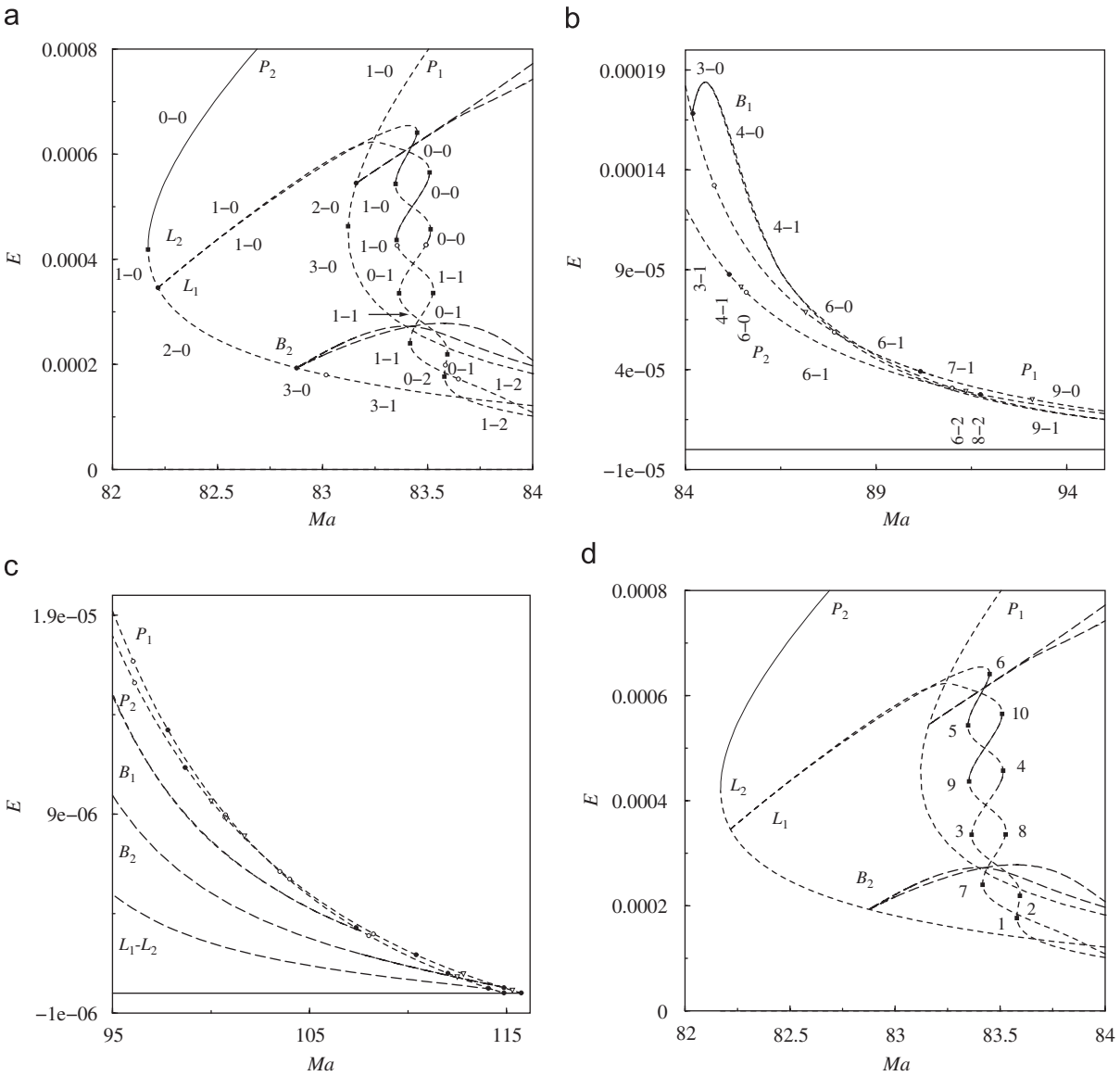

Fig. 5. (a)–(c) Bifurcation diagrams showing the velocity norm for time-independent solutions in three different ranges of the Marangoni number *Ma*, together with the stability assignments with respect to perturbations preserving the reflection symmetry *R*. In (b) only some of the branches are shown. (d) Labeled saddle-nodes on the branches L_1 and L_2 of localized states used in Fig. 6. Solid (dashed) lines indicate stable (unstable) solutions. Parameters are $Sc = 50$, $Pr = 1$, $S_M = -0.005$, $\Gamma = 10\lambda_c$, where $\lambda_c = 3.1$ is the critical wavelength for the onset of convection in a pure fluid. Resolution is $N_e = 20$–22, $N_x = N_z = 17$.

large scale modulation of the spatially periodic state P_2, and both branches terminate together just below the saddle-node on the P_2 branch (Fig. 5a). Once again the upflow state terminates on the P_2 state with upflow at $x = \Gamma/2$, while the downflow state terminates on the half-wavelength translate of this state, characterized by downflow at $x = \Gamma/2$.

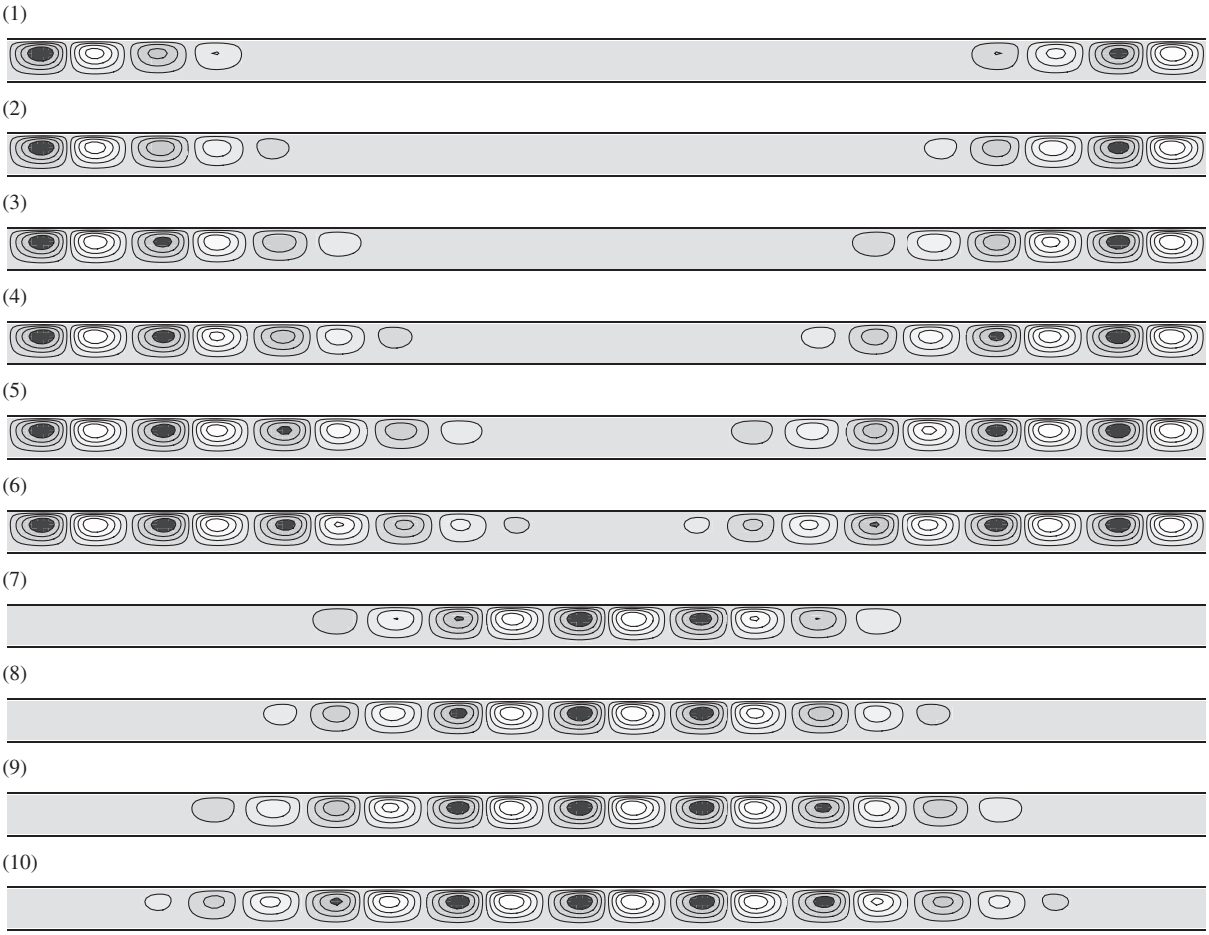

Fig. 6. Solutions in the neighborhood of the saddle-nodes on the snaking branches L_1 (1)–(6) and L_2 (7)–(10). (1) $Ma = 83.6271$, (2) $Ma = 83.5935$, (3) $Ma = 83.3641$, (4) $Ma = 83.5138$, (5) $Ma = 83.3466$, (6) $Ma = 83.4447$, (7) $Ma = 83.4166$, (8) $Ma = 83.5254$, (9) $Ma = 83.3536$ and (10) $Ma = 83.4819$. The L_2 states are distinct from $\Gamma/2$ translates of the L_1 states.

The stability properties of the steady localized states with respect to R-symmetric perturbations are summarized in Fig. 5a. The figure shows that while throughout most of their region of existence the localized states are unstable, there are intervals of parameter values within the snaking or pinning region in which these can indeed be stable. The stable segments lie between adjacent saddle-nodes and have positive slope, much as occurs in systems with variational structure (Burke and Knobloch, 2006). However, lower down the snaking branches the localized states lose stability with respect to R-symmetric *oscillations*, eliminating some of the stable segments. This situation occurs on the branch L_1. The associated Hopf bifurcation appears to be subcritical since no stable R-symmetric oscillations were located near the Hopf bifurcation, and the system evolves towards P_2 as the final state. The corresponding bifurcation on the L_2 branch occurs on a branch segment that is already unstable. In other systems with nonvariational structure the stability properties are similar but spatially localized oscillations are found instead (Yochelis et al., 2006).

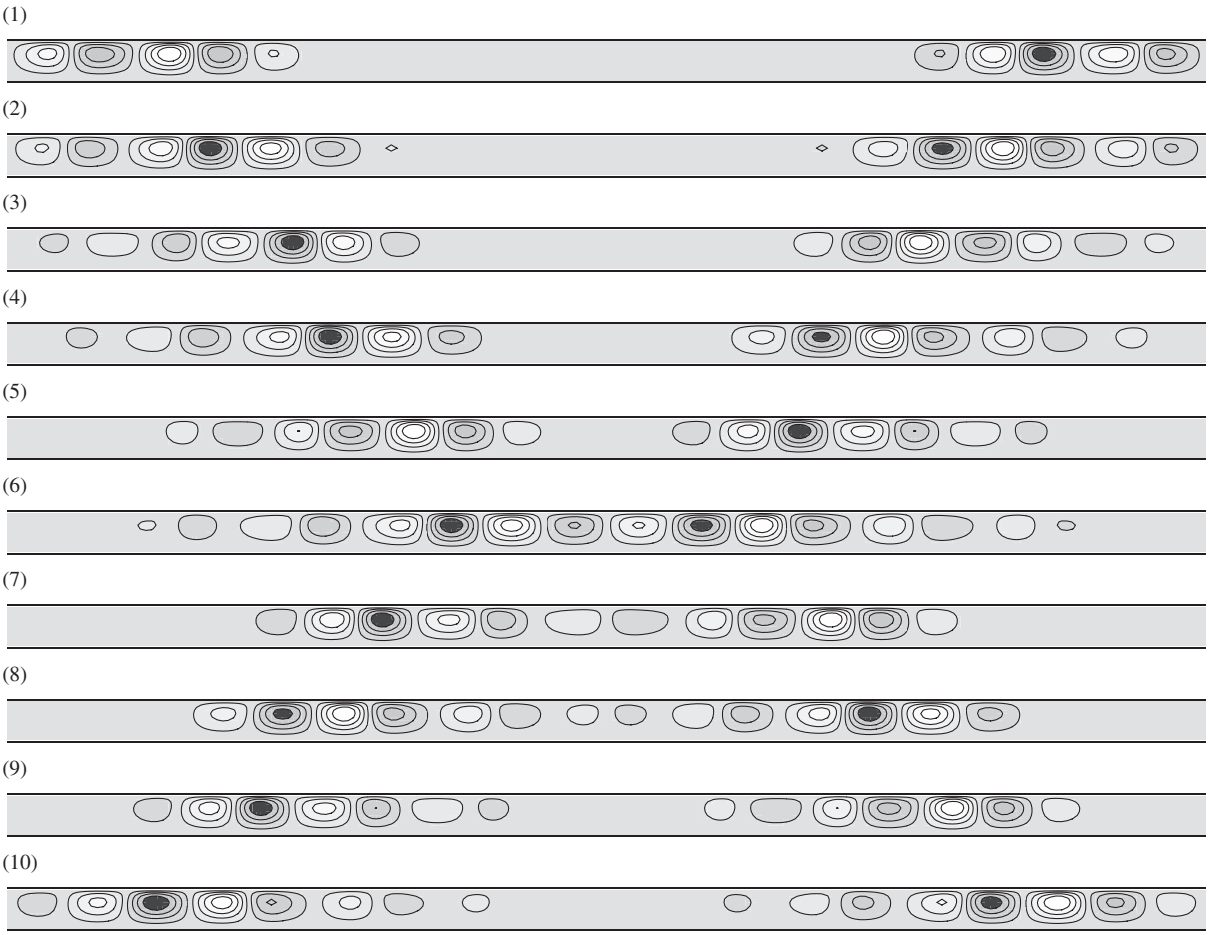

Fig. 7. Eigenmodes associated with the saddle-nodes of the snaking branches L_1 (1)–(6) and L_2 (7)–(10). (1) $Ma = 83.6271$, (2) $Ma = 83.5794$, (3) $Ma = 83.3652$, (4) $Ma = 83.5122$, (5) $Ma = 83.3512$, (6) $Ma = 83.4414$, (7) $Ma = 83.4166$, (8) $Ma = 83.5246$, (9) $Ma = 83.3549$ and (10) $Ma = 83.4673$.

Fig. 7 shows the eigenfunctions close to the saddle-node bifurcations labeled in Fig. 5d, corresponding to the states in Fig. 6. These eigenfunctions are R-symmetric and correspond to modes that are neutrally stable at the saddle-nodes. The figure reveals that the eigenfunctions are localized near the fronts at either end of the localized states, and are responsible for the nucleation of new rolls that lead to the growth of the structure as one proceeds up the snaking curve.

The stability properties summarized in Fig. 5a depend on the imposed symmetry R. If this requirement is relaxed the stability properties may change. We find that while the L_1 states remain stable between saddle-nodes (5) and (6), the L_2 states are now only stable in a very small interval of Marangoni numbers between saddle-nodes (9) and (10), bounded on the left by a Hopf bifurcation and on the right by a parity-breaking bifurcation that produces (unstable) asymmetric localized states that drift either to the left or the right. Neither bifurcation is shown in the figure. The Hopf bifurcation, like the parity-breaking bifurcation, breaks the R-symmetry, and results in the appearance of standing oscillations in the wings

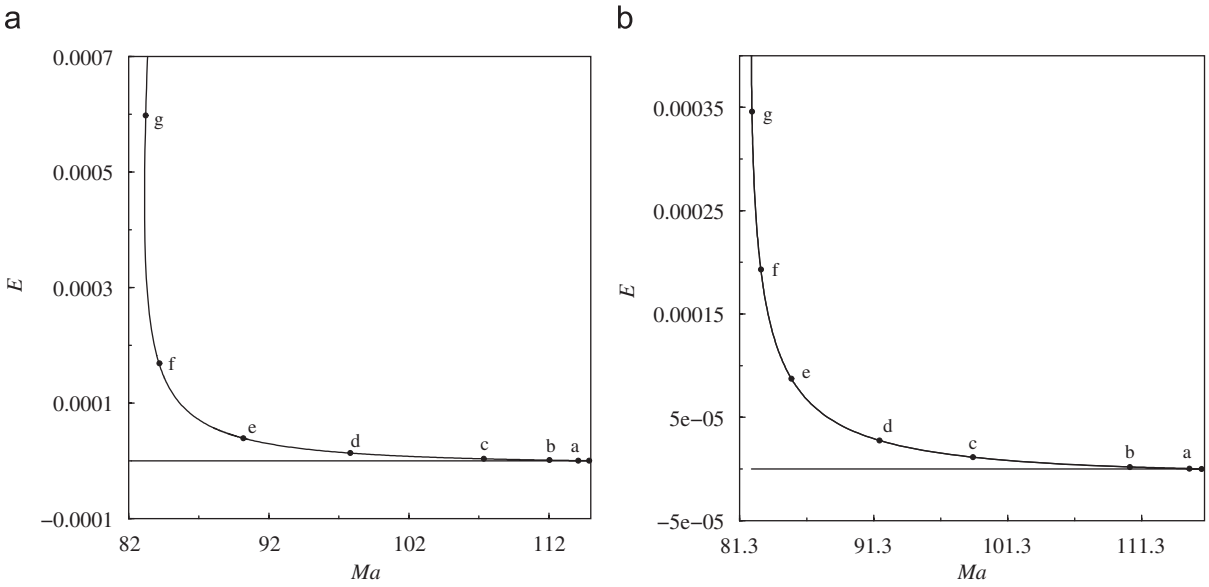

Fig. 8. Bifurcation diagram showing the location of secondary bifurcations, labeled a–g, along (a) branch P_1, (b) branch P_2. Parameters are $Sc = 50$, $Pr = 1$, $S_M = -0.005$ and $\Gamma = 10\lambda_c$. Resolution is $N_e = 20$, $N_x = N_z = 17$.

of the solution that are *exactly* out of phase. Solutions of this type are discussed in greater detail in the following section.

The linear stability results for the P_1 and P_2 branches with respect to R-symmetric perturbations, summarized in Figs. 5a–c, indicate the presence of additional secondary steady state bifurcations. Since both branches consist of very similar states their stability properties are also similar (Fig. 8). Fig. 9 shows the marginally stable eigenfunctions along P_1. The eigenfunction a is responsible for triggering the small amplitude instability leading to the snaking branches L_1, L_2; when added to P_1 it produces a pattern with wavenumber $n = 11$ modulated by a wavenumber 1 perturbation. The succeeding bifurcations also lead to wavelength modulation. For example, the bifurcations at c and f mark the beginning and end of the secondary branches labeled B_1 in Fig. 5b. Fig. 10 shows a solution on one of these branches near the location f. Finally, solution g shows that a secondary branch consisting of nine pairs of rolls bifurcates from P_1 just above the saddle-node. We have not followed all of these secondary branches, nor examined their stability properties; however, the branches B_1 are unstable throughout.

In contrast, the corresponding bifurcation at a on P_2 (Fig. 11) produces a pair of branches B_2 with admixture of wavenumber 12, which terminate back on P_2 at f. These branches are also unstable throughout. A sample solution on one of these branches near f is also shown in Fig. 10. The bifurcation at g corresponds to the termination of the snaking branches L_1, L_2 (cf. Fig. 9a).

3.2.2. Time-dependent states

We now turn to time-dependent states. For the parameter values used the conduction state loses stability to a Hopf bifurcation at $Ma \approx 80.92$ just before the saddle-node bifurcation on the P_2 branch at $Ma \approx 82.16$. This is very close to the result for the infinite layer ($\Gamma \to \infty$), for which the critical Marangoni number $Ma_H \approx 80.9003$, corresponding to the wavelength $\lambda_H \approx 3.152$ and frequency $\omega_H \approx 0.3675$.

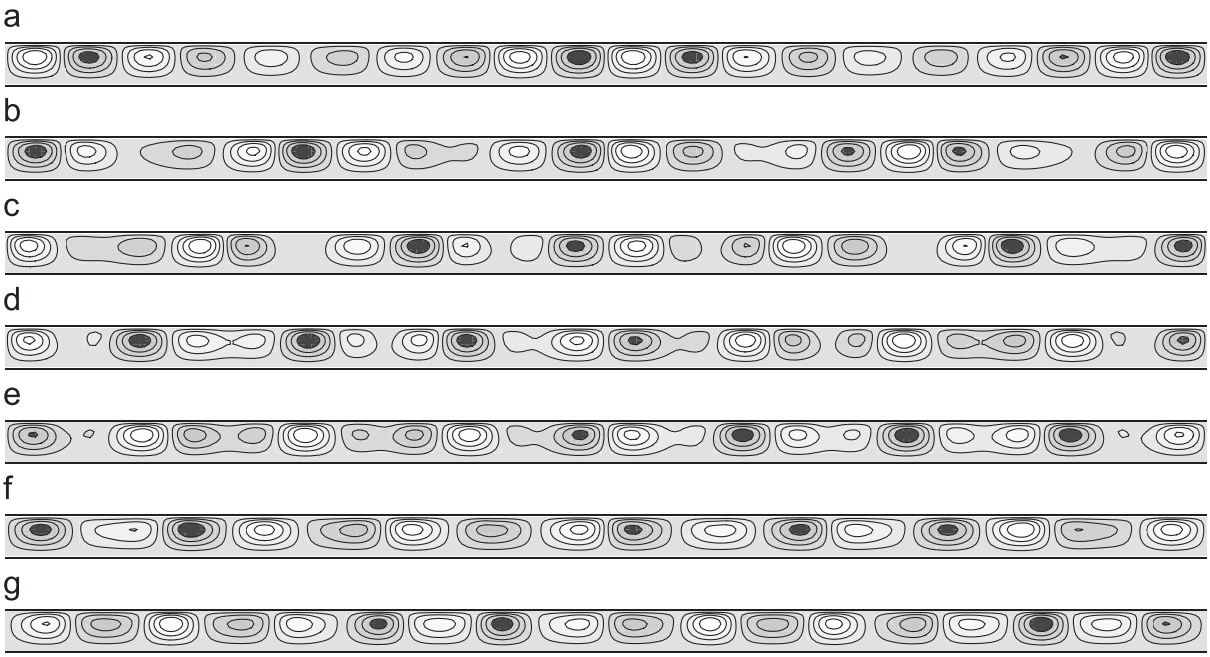

Fig. 9. Eigenmodes associated with the different secondary bifurcations along the P_1 branch (Fig. 8a). Parameters are $Sc = 50$, $Pr = 1$, $S_M = -0.005$, $\Gamma = 10\lambda_c$, with (a) $Ma = 114.2958$, (b) $Ma = 112.1941$, (c) $Ma = 107.6806$, (d) $Ma = 98.4211$, (e) $Ma = 90.3703$, (f) $Ma = 84.1869$ and (g) $Ma = 83.1399$. Resolution is $N_e = 20$–22, $N_x = N_z = 17$.

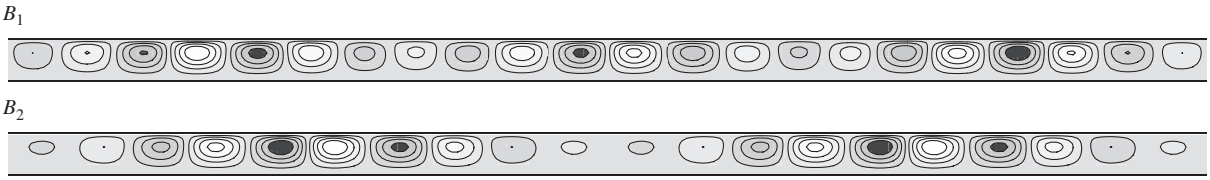

Fig. 10. Solutions on one of the B_1 and one of the B_2 branches near their termination points closest to the saddle-nodes on P_1, P_2. Parameters are $Ma = 84.4711$ (B_1), $Ma = 83.6335$ (B_2), $Sc = 50$, $Pr = 1$, $S_M = -0.005$ and $\Gamma = 10\lambda_c$. Resolution is $N_e = 20$–22, $N_x = N_z = 17$.

In this regime one must find time-dependent states, and indeed one finds that the Hopf bifurcation is supercritical and evolves into a pattern of stable standing waves (hereafter SW, see Fig. 12). With increasing Ma there is a hysteretic transition to stable traveling waves (hereafter TW, see Fig. 13a). Both branches are produced in the same primary Hopf bifurcation, and both have the same spatial wavenumber $n = 10$. The TW branch (not shown) goes through a saddle-node bifurcation at $Ma \approx 82.367$ at which it turns towards smaller values of Ma, but not before losing stability to a spatially modulated state at $Ma \sim 82.20$ (Fig. 13b). With further increase in Ma these states lose stability and the system evolves, after a long and complex transient involving transitions between both left and right TW and SW to the spatially periodic $n = 10$ steady state P_2. With increasing Ma these transients involve the episodic

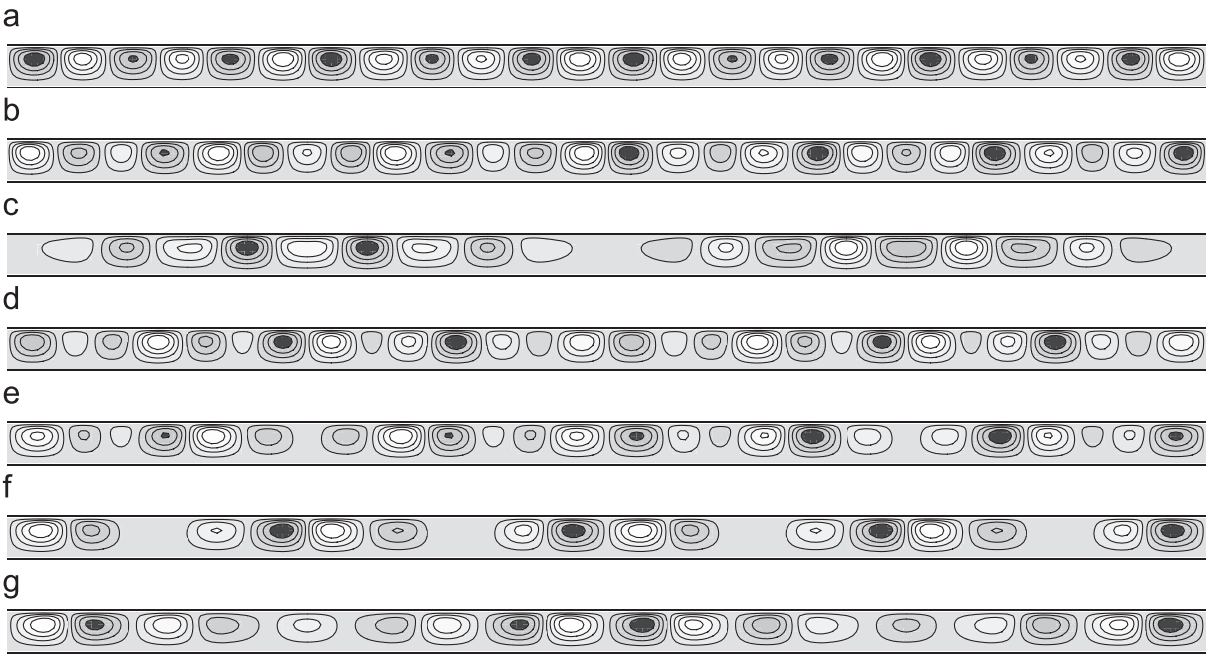

Fig. 11. Eigenmodes associated with the different secondary bifurcations along the P_2 branch (Fig. 8b). Parameters are (a) $Ma = 114.8119$, (b) Ma=110.1928, (c) $Ma = 98.6935$, (d) $Ma = 92.1226$, (e) $Ma = 85.2025$, (f) $Ma = 82.8894$ and (g) $Ma = 82.2163$. Resolution is $N_e = 20$–22, $N_x = N_z = 17$.

creation of spatially localized steady states, but the system eventually always reaches the P_2 state. Fig. 14 shows two snapshots of a typical transient observed at $Ma = 83.15$. Observe that the localized structures form intermittently and occur spontaneously in various parts of the domain. This is in contrast to the case of binary fluid mixtures where the small Lewis number results in the presence of a slow field (the concentration) that produces a memory effect that in turn favors creation of localized structures always in the same location. Since these states are almost stationary they collapse initially to the unstable SW which are in turn unstable to TW disturbances, an instability inherited from lower values of Ma (Fig. 13a), before the process repeats. The observed behavior is undoubtedly a consequence of the absence of the TW branch at these Marangoni numbers, together with the conjectured absence or instability of the associated modulated TW. As a result there is an interval in Marangoni number in which all solutions evolve to the stable steady spatially periodic states P_2 on the upper branch, but necessarily do so via a complex transient of the type shown in Fig. 14. The resulting evolution is similar to that found in binary fluid convection where the unstable SW decay into dispersive chaos, a state that appears to be locally 'unstable' to the formation of localized structures but globally 'stable'.

As Ma is increased the incipient localized states persist for longer and longer times, until the localized structures persist apparently indefinitely. Interestingly, the Marangoni number at which this first occurs ($Ma \approx 83.175$) lies substantially *below* the value corresponding to the presence of the saddle-node bifurcations on the L_1, L_2 branches identified in Fig. 5, viz. $Ma \approx 83.35$. It appears that this is so because the first spatially localized states that appear are not in fact time-independent. Fig. 15 shows two distinct localized states both found at $Ma = 83.20$. Both states are embedded in a background of small amplitude

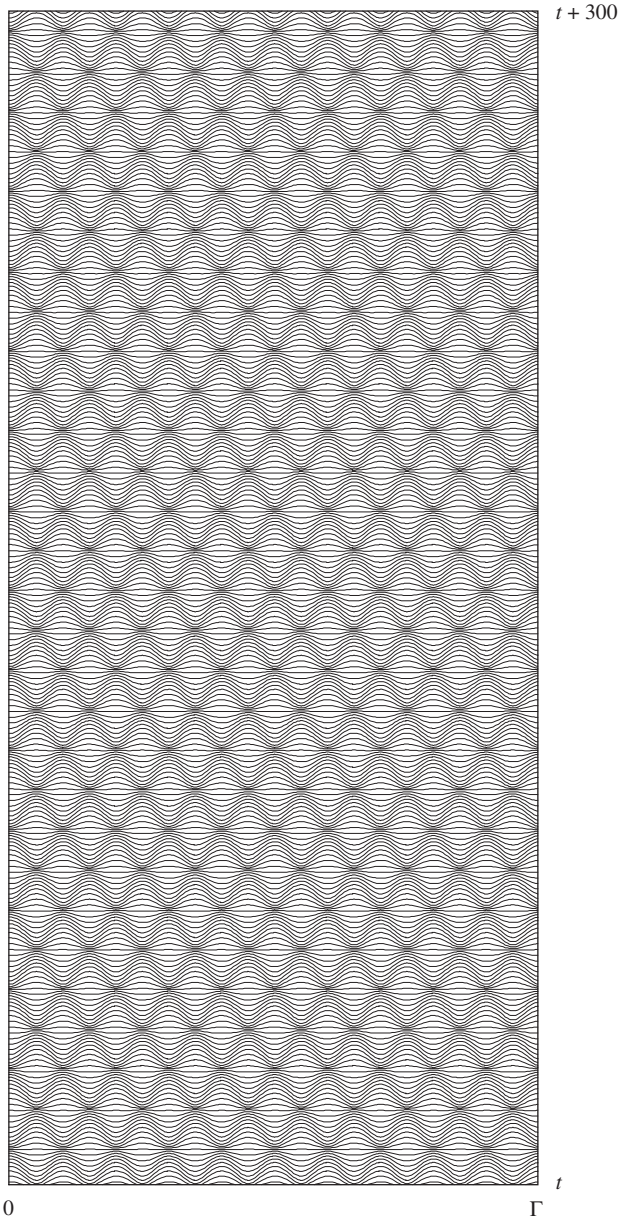

Fig. 12. Space–time plot showing the vertical velocity in the midplane for a stable standing wave solution at $Ma = 82.0$.

SW that are preferred over TW in the small domains left over by the localized state. The first of these states consists of two dominant pairs of rolls with downflow in the middle, while the second consists of three pairs of rolls with upflow in the middle. Both structures are almost time-independent and appear to be sustained by the small amplitude background SW. In both cases the overall state is periodic in time, and numerically stable. Note that the SW on the two sides are exactly out of phase, implying that the

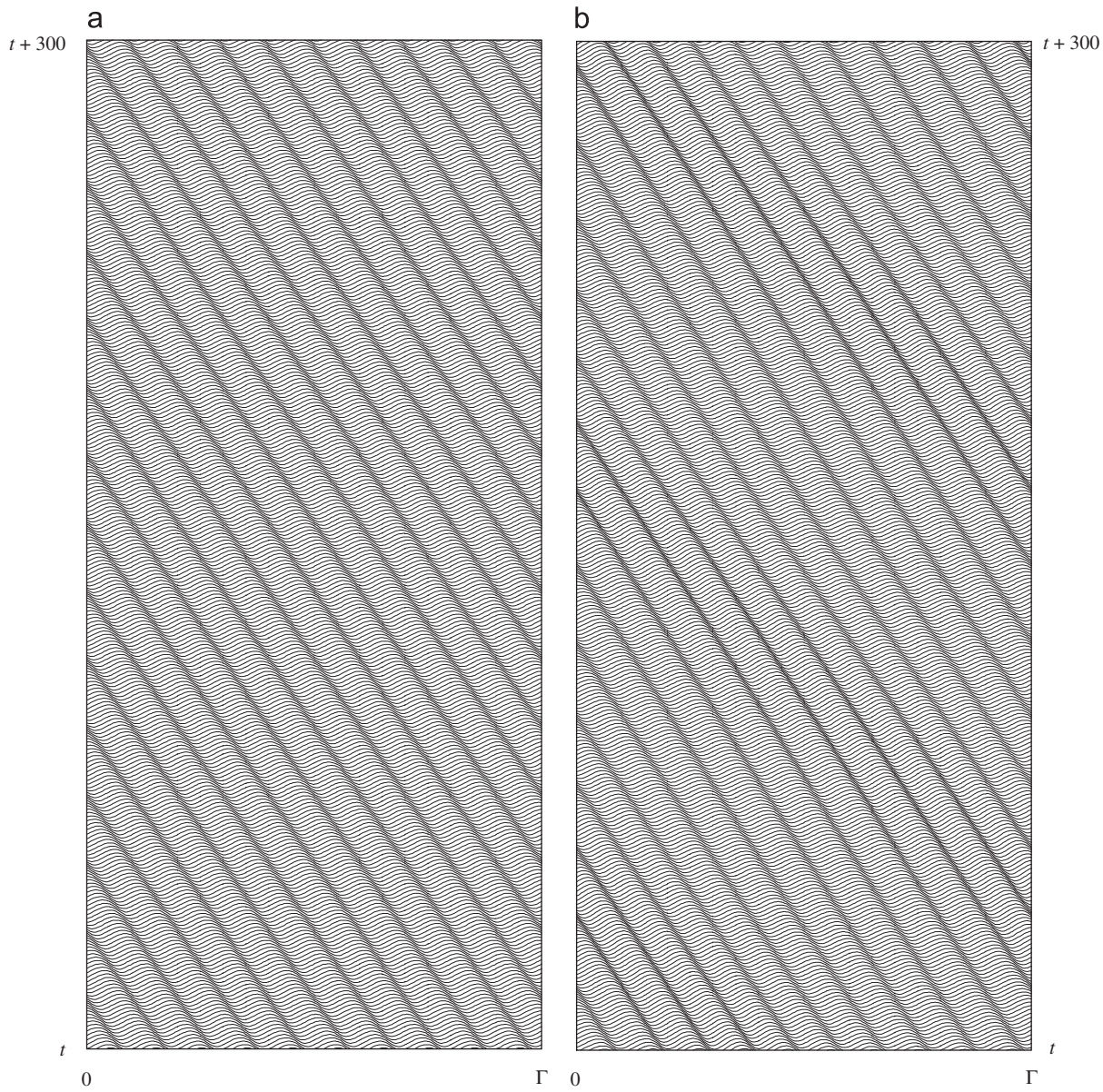

Fig. 13. Space–time plot showing (a) a stable left-traveling wave and (b) a stable modulated traveling wave solution at $Ma = 82.10$ and 82.35, respectively.

whole structure executes small back and forth oscillations. We conjecture that states of this type become possible once the SW in the domain outside the localized state acquire stability, i.e., only for convectons that are sufficiently broad. As Ma increases the bistability between states with odd and even numbers of roll pairs persists but the localized states gradually broaden. For example, at $Ma = 83.35$ (Fig. 16) the state in Fig. 15a has added a roll on either side while the state in Fig. 15b remains qualitatively unchanged.

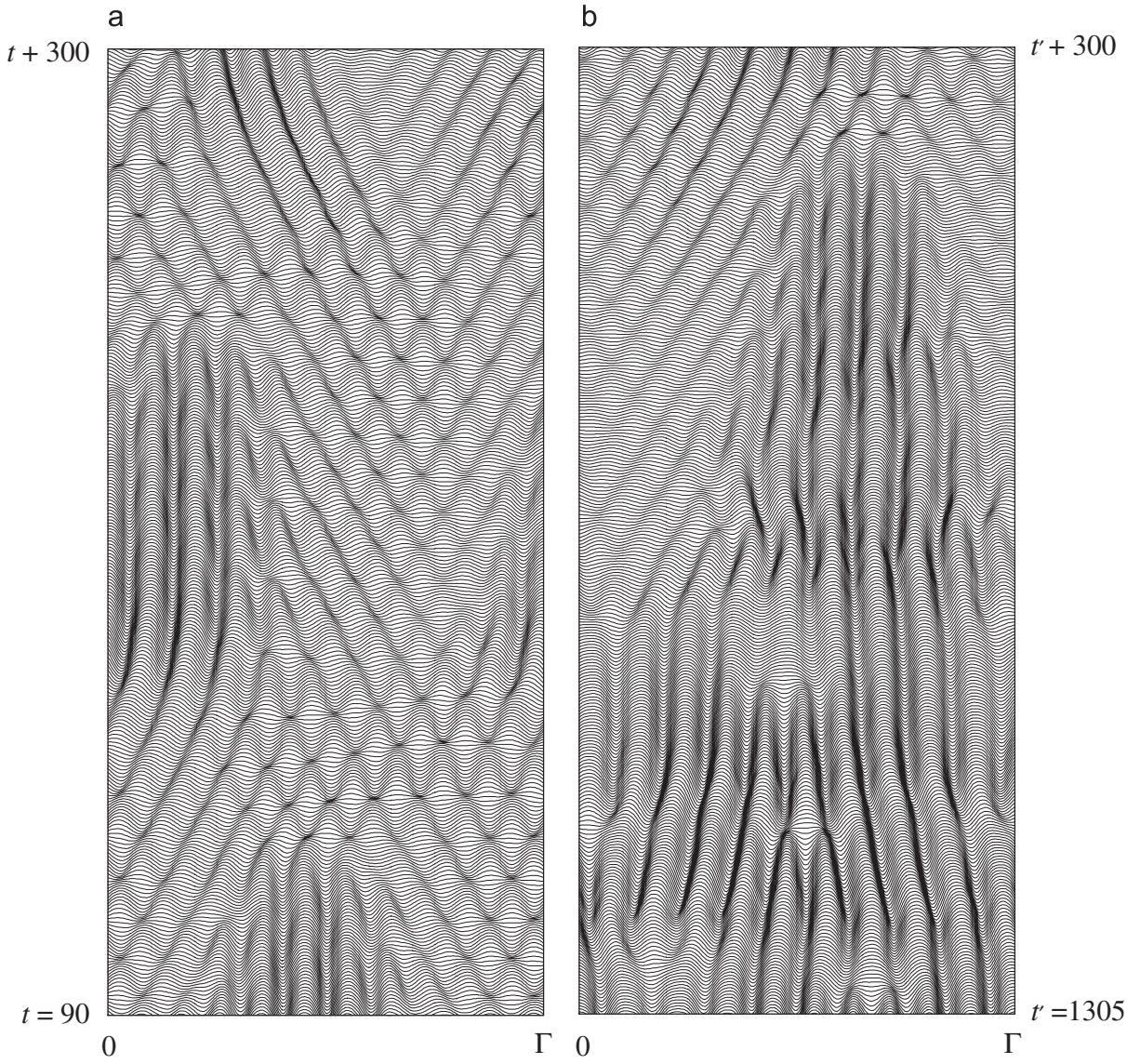

Fig. 14. Two segments of a space–time plot of the transient at $Ma = 83.15$, showing the episodic generation of spatially localized structures followed by their collapse into small amplitude standing waves that are in turn unstable to traveling wave perturbations.

Throughout this process the sustaining waves on either side remain out of phase and periodic in time, while their amplitude (and period) gradually decreases. Despite the evident hysteresis between the upflow and downflow states that echoes that present for the time-independent spatially localized states (Fig. 5) the transitions that preserve upflow or downflow in the center appear to be largely nonhysteretic. The overall picture suggests the presence of snaking for *time-periodic* spatially localized states resembling that already described for time-independent states (Fig. 5).

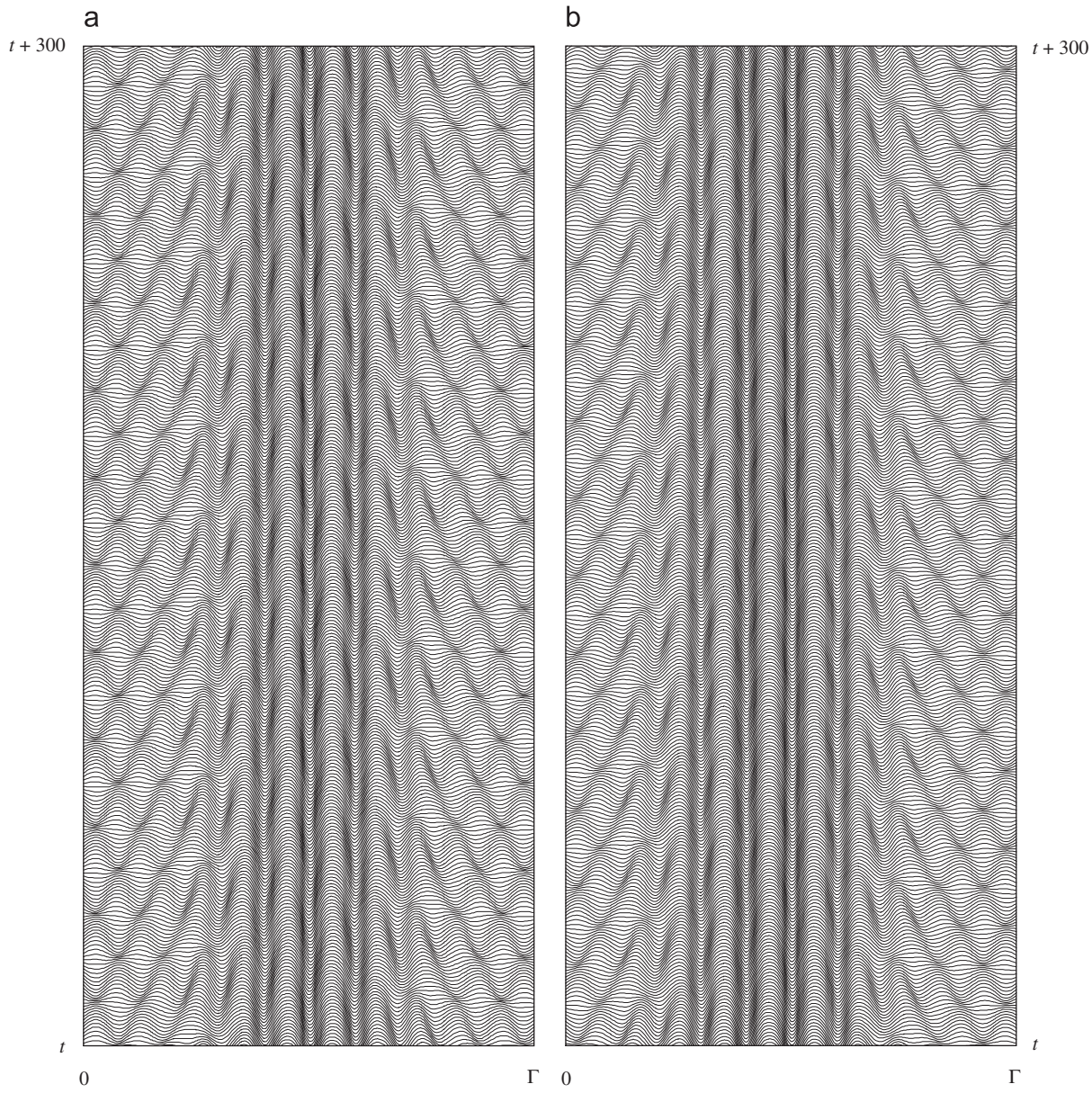

Fig. 15. Space–time plots of two distinct convectons in a background of standing waves at $Ma = 83.20$. State (a) consists of two roll pairs with downflow in the center; while (b) consists of three roll pairs with upflow in the center. Both states are strictly periodic in time.

Fig. 17a shows a broader localized structure with downflow in the center obtained at $Ma = 83.45$, starting from a narrower solution at $Ma = 83.40$ resembling Fig. 16a. This structure is still sustained by the surrounding waves, in agreement with the stability results for steady upflow and downflow states described in the preceding section, although the amplitude of the waves is now quite small. In contrast,

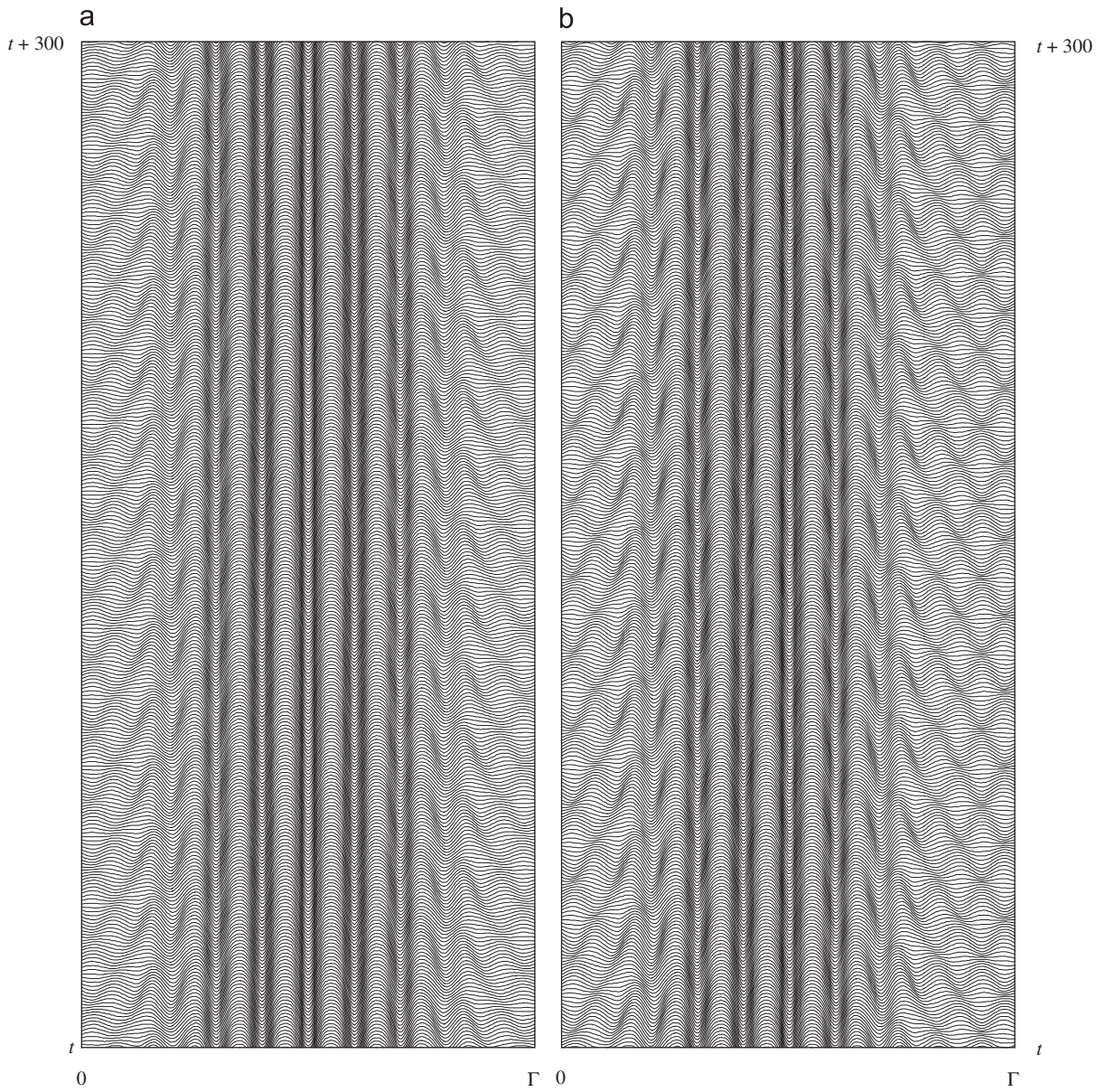

Fig. 16. Space–time plots of two distinct convectons in a background of standing waves at $Ma = 83.35$. Both states are strictly periodic in time.

when $Ma = 83.40$ we have found a localized structure with upflow in the center but no sustaining SW (Fig. 17b). This state is therefore an example of one of the stable localized steady states present on the L_1 branch in Fig. 5, and was obtained here from the narrower wave-sustained upflow state at $Ma = 83.35$ (Fig. 16b) by increasing Ma. On the other hand starting from this solution and increasing Ma to 83.50 led to an instability in which the pattern rapidly nucleates new rolls at either side and evolves towards

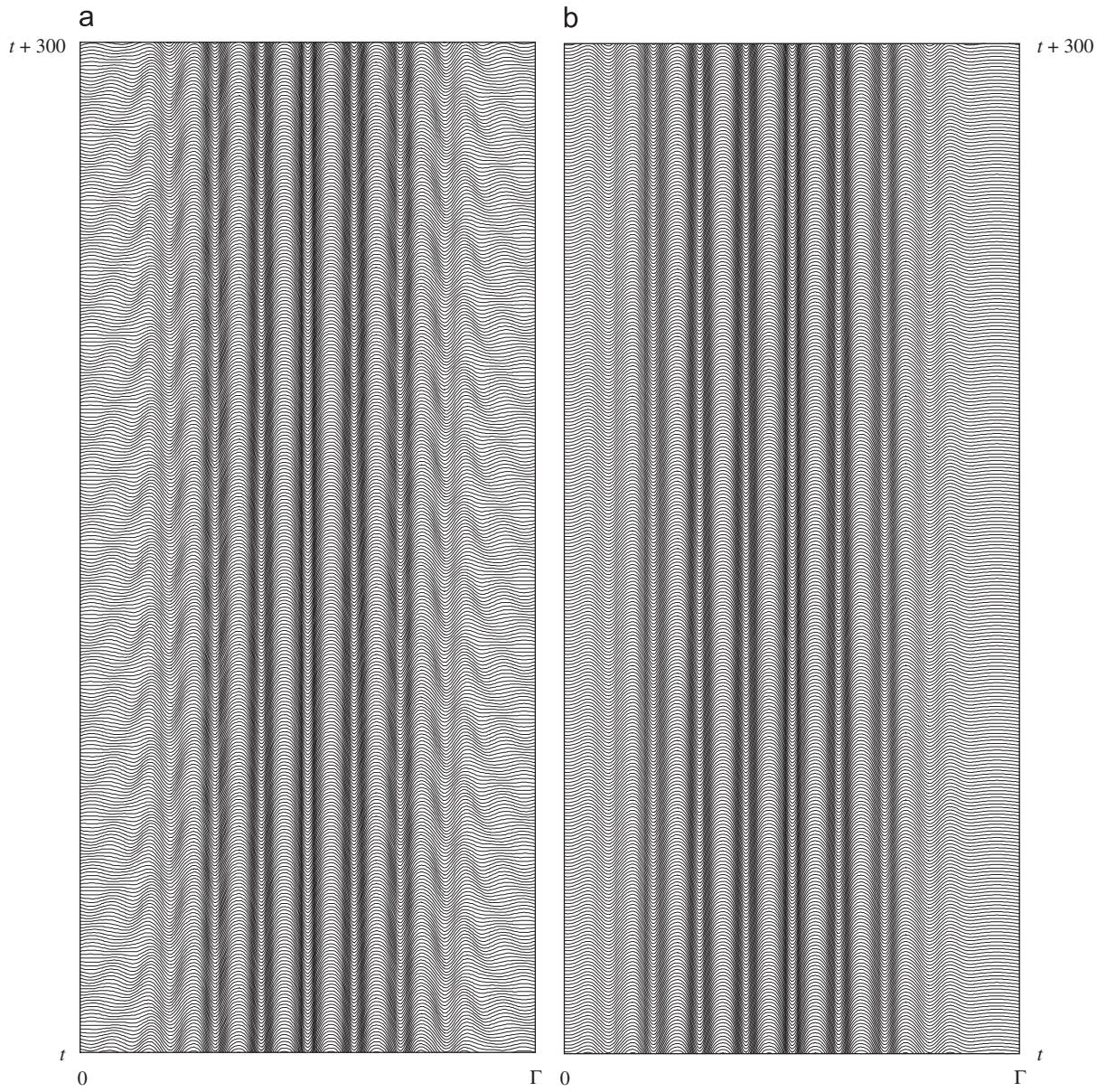

Fig. 17. Space–time plots of convectons at (a) $Ma = 83.45$ and (b) $Ma = 83.40$. In (b) no background waves are present.

the P_2 state, a result that is consistent with Figs. 5 and 6. Note in particular that in the pinning region identified in Fig. 5 the convectons are stable despite connecting to a conduction state that is unstable to growing oscillations. Despite this for some parameter values (e.g., $Ma = 83.40$) no waves are visible in direct numerical simulations (Fig. 17b).

It is noteworthy that as Ma increases the amplitude of the background decreases. This unexpected aspect of the problem is a consequence of the relatively small spatial period Γ used in the calculations.

As already mentioned the preferred length $L_{\rm loc}$ of the localized states decreases with decreasing Ma, and consequently the length $L_{\rm w} \equiv \Gamma - L_{\rm loc}$ of the domain supporting waves grows. Since the critical Marangoni number for the onset of an oscillatory instability in a domain of length $L_{\rm w}$ decreases with increasing $L_{\rm w}$ (Bergeon et al., 2003) the background state is in fact more supercritical for lower values of Ma than for higher values for which the background region is quite narrow and the threshold Marangoni number therefore high. Of course once Ma is increased past the snaking region steady localized states no longer exist, and the convectons grow in length by nucleating rolls symmetrically at either end until the domain is filled, much as in other systems of this type (Batiste et al., 2006; Bergeon and Knobloch, 2007).

In the following section we provide an interpretation of these results.

4. Discussion and conclusions

In this paper we have identified the presence of stable spatially localized states in Marangoni convection in a binary mixture when the separation ratio is negative. The requirement $S_M < 0$ is responsible for the subcriticality of the primary steady branches and hence for the presence of 'bistability' between the conduction state and spatially periodic states required for the existence of a pinning or snaking region in spatially reversible systems on the real line.

The localized states we have found emerge from a parameter regime associated with long transients, and are typically embedded in a background of SW, in contrast to similar states present in variational systems. States of this type are present for $83.175 < Ma < 83.50$; related states been seen in experiments by Kolodner on water–ethanol mixtures in a narrow annulus (Kolodner, 1993; Kolodner et al., 1995), as well as in numerical simulations of He^3–He^4 mixtures (Batiste and Knobloch, 2005) and water–ethanol mixtures (Batiste et al., 2006; Alonso et al., 2007). In these systems, like in the present one, stable convectons are found in a regime in which the background conduction state is unstable to oscillations. In binary mixtures this fact is now understood as being due to the fact that the conduction state is only convectively unstable, while remaining stable with respect to absolute instability. Batiste et al. (2006) and Alonso et al. (2007) show that when the absolute instability threshold is exceeded the region between adjacent convectons fills with TW, a consequence of the instability of weakly nonlinear SW to TW. Thus in binary fluid convection above the absolute instability threshold convectons are embedded in a background of TW, and this state is present for larger forcing than the TW-free state. In contrast, in the present system the situation appears to be reversed: when the convectons first appear they are embedded in a background of SW, and these SW disappear with *increasing* Marangoni number. However, in the present system the explanation for the observed behavior is quite different. The convectons are embedded in a background of SW since these waves are stable with respect to TW perturbations in the domains considered. The distinction between convective and absolute instability does not enter the discussion since no propagating disturbances are involved. Instead the SW background gradually disappears for the simple reason that the localized states broaden and the remainder of the domain becomes subcritical for oscillatory instability. Whether these conclusions carry over to larger domains requires computations in much larger domains, and these do not currently permit stability computations that have proved so useful in the present work.

Despite their complexity the phenomena described in the preceding section have a simple explanation. This explanation is based on the observation that with increasing spatial period Γ the secondary pitchfork bifurcation on the P_1 branch moves to smaller and smaller amplitude; at the same time the primary bifurcations corresponding to the branches P_1 and P_2 approach a common bifurcation value. Thus in the

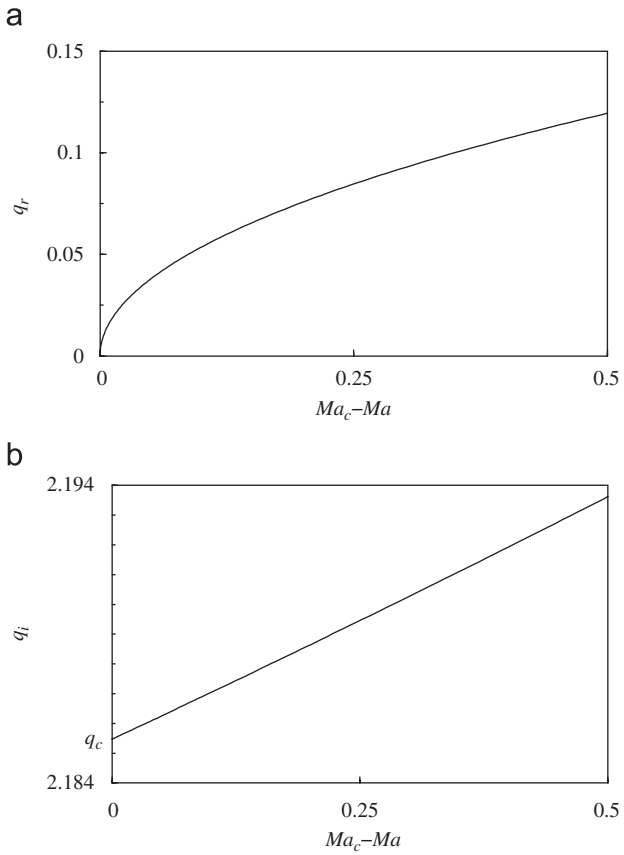

Fig. 18. The (a) real and (b) imaginary parts of the spatial growth rate q as a function of the Marangoni number Ma near onset of the primary steady state instability on the real line.

limit $\Gamma \to \infty$ all these bifurcations coincide with the point $Ma \equiv Ma_c$ that corresponds to the minimum of the neutral stability curve for stationary perturbations, and the spatially localized states bifurcate directly from the conduction state. This minimum in turn defines the (real) wavenumber q_c selected by linear theory in an unbounded domain, and hence the wavelength $2\pi/q_c$ of the spatially periodic state that results from the stationary instability. On the other hand this wavenumber need not be the preferred wavenumber in the nonlinear regime. The behavior at the upper end of the snaking branches is more complex, and depends, in general, on the choice of the spatial period Γ (Bergeon et al., 2008): the branches can either terminate together on the same branch of periodic states as in Fig. 5 and do so below or above the saddle-node, or separately on different branches periodic states, or indeed not terminate at all.

To show that in an infinite domain the time-independent spatially localized states bifurcate *directly* from the conduction state we solve the linear stability problem on the real line, i.e., we look for solutions proportional to $\exp qx$, and solve for the spatial eigenvalues q. We compute only the four eigenvalues whose real part passes through zero as Ma passes through $Ma_c \approx 114.806$, the threshold for the onset of the primary steady state instability on the real line. Fig. 18 shows that near $Ma > Ma_c$ the four important eigenvalues all lie on the imaginary axis while for $Ma < Ma_c$ these eigenvalues form a quartet in the

complex q plane. At the same time the imaginary part (the spatial wavenumber) varies linearly with Ma. This eigenvalue structure is a consequence of the spatial reversibility R of Eqs. (1)–(5). At $Ma = Ma_c$ there is a pair of purely imaginary eigenvalues $\pm iq_c \approx \pm 2.18547i$ of double multiplicity, corresponding to wavelength $\lambda_c \approx 2.8749$. Evidently exponentially localized states, i.e., states that depart from the conduction state as x increases from $x = -\infty$ and return to it as $x \to \infty$ can only be present for $Ma < Ma_c$, where the conduction state is hyperbolic. Under these conditions it is possible to demonstrate the existence of such states by examining the neighborhood of the 1:1 reversible Hopf bifurcation that takes place at $Ma = Ma_c$ (Champneys, 1998; Burke and Knobloch, 2006). The theory shows that both periodic states *and* two branches of distinct localized states bifurcate generically from the conduction state at $Ma = Ma_c$, and that both do so in the same direction, in the present case subcritically. Near a particular codimension two point this approach can capture the snaking region as well (Kozyreff and Chapman, 2006).

As Ma decreases the localized states produced at Ma_c contract to an $O(1)$ width and grow to an $O(1)$ amplitude, before beginning to snake. In the limit of infinitely large Γ the localized states high up the 'snake' resemble a bound state of two fronts, the left one connecting the conduction state to the spatially periodic state and vice versa on the right. A state of this type corresponds to the simultaneous formation of a pair of heteroclinic connections, between the conduction state and the periodic state, and back to the conduction state. These connections are related by the symmetry R, and correspond to the bounding fronts. Such pairs of heteroclinic connections are present throughout the snaking region. In variational systems the presence of the resulting time-independent structures can be attributed to the *pinning* of the bounding fronts to the periodic structure within. It is this pinning that is responsible for the multiplicity of time-independent spatially localized states within the snaking region, as well as for its finite extent in the Marangoni number Ma.

In variational systems the snaking or pinning region is organized around the so-called Maxwell point at which the spatially periodic state has the same energy as the conduction state. As a result the pinning region can be thought of as the broadening of the Maxwell point due to the pinning of the fronts at either end of the localized states to the periodic structure within. Moreover each localized state is characterized by different energy, although all stable localized states correspond to local energy minima. In the presence of noise the system can 'tunnel' from higher 'metastable' minima to minima with lower energy, i.e., from wider localized states to narrow localized states. The tunneling rate depends of course on the noise level as well as on the energy difference between adjacent states. As the Marangoni number is decreased shorter, more compact convectons, become energetically preferred, and the incident waves push the system in this direction (Sakaguchi and Brand, 1996; Aranson et al., 2000; Clerc et al., 2005). Thus the wave background is responsible for selecting, at each value of the Marangoni number, a (stable) localized state with upflow in the center and a (stable) localized state with downflow in the center, each with a *preferred* length. Related behavior has been noted in experiments on buoyancy-driven convection in binary fluids (Kolodner, 1993); indeed, we expect our results to describe qualitatively the corresponding Marangoni–Bénard problem provided buoyancy effects remain weak. It is of interest to note that in stochastic variational systems the location of the resulting 'phase transition' is also determined by a Maxwell construction (Sastry and Hijab, 1981).

It is perhaps unexpected that the behavior of the present system is so similar to that of binary fluid convection and natural doubly diffusive convection. Evidently this is so because all three systems are spatially reversible in the appropriate sense, all three exhibit subcritical bifurcations to spatially periodic states thereby generating bistability between the conduction state and a spatially periodic state. All the

systems are also of sufficiently high order in the extended variable that they exhibit a reversible Hopf bifurcation with 1:1 resonance (in space). An example is described in Fig. 18. Under these conditions spatially localized states bifurcate from the primary bifurcation point and do so subcritically as well. The snaking region is the result of a transverse intersection between the unstable manifold of the conduction state (in space) and the stable manifold (in space) of the periodic state viewed as a periodic orbit in phase space. Once this structure forms the rest of the behavior follows. Moreover, in cases where the primary steady state bifurcation is preceded by a Hopf bifurcation, the snaking region is preceded by relaxation oscillations, and destroyed by the unpinning of the bound fronts as the forcing increases. In some cases the latter transition may be complicated by the presence of waves between adjacent convectons, but the presence of such waves is largely benign, and can be understood on the basis of simple linear notions. Indeed, we may think of the waves as a superposition of left- and right-TW of the form

$$\mathrm{Re}\{A(x)\,\mathrm{e}^{\mathrm{i}kx+\mathrm{i}\omega t} + B(x)\,\mathrm{e}^{-\mathrm{i}kx+\mathrm{i}\omega t}\}, \tag{7}$$

where $A(x)$, $B(x)$ are complex amplitudes. The numerical results shown in Figs. 15 and 16 indicate that away from the convecton $|A(x)|$, $|B(x)|$ become equal, producing standing oscillations, while near the left (right) boundary $|B(x)| > |A(x)|$ ($|B(x)| < |A(x)|$) indicating that right-TW dominate near the left boundary, while left-TW dominate near the right boundary. Thus the waves always impinge *on* the convecton thereby helping to sustain the state even outside the pinning region.

Acknowledgments

This work was supported in part by a CNRS Projet International de Cooperation Scientifique (PICS 3471) and by the National Science Foundation under Grant DMS-0605238. We are grateful to J. Burke for helpful discussions.

References

Alonso, A., Batiste, O., Meseguer, A., Mercader, I., 2007. Complex dynamical states in binary mixture convection with weak negative Soret coupling. Phys. Rev. E 75, 026310.

Aranson, I.S., Malomed, B.A., Pismen, L.M., Tsimring, L.S., 2000. Crystallization kinetics and self-induced pinning in cellular patterns. Phys. Rev. E 62, R5.

Batiste, O., Knobloch, E., 2005. Simulations of localized states of stationary convection in ^{3}He–^{4}He mixtures. Phys. Rev. Lett. 95, 244501.

Batiste, O., Knobloch, E., Alonso, A., Mercader, I., 2006. Spatially localized binary-fluid convection. J. Fluid Mech. 560, 149.

Bergeon, A., Knobloch, E., 2004. Oscillatory Marangoni convection in binary mixtures in square and nearly square containers. Phys. Fluids 16, 360.

Bergeon, A., Knobloch, E., 2007. Spatially localized states in natural doubly diffusive convection. Phys. Fluids, in press.

Bergeon, A., Henry, D., Ben Hadid, H., 1994. Marangoni–Bénard instability in microgravity conditions with Soret effect. Int. J. Heat Mass Transfer 37, 1545.

Bergeon, A., Henry, D., Ben Hadid, H., 1995. Analytical linear stability analysis of Marangoni instability with Soret effect. Microgravity Q 37, 123.

Bergeon, A., Henry, D., Ben Hadid, H., Tuckerman, L.S., 1998. Marangoni convection in binary mixtures with Soret effect. J. Fluid Mech. 375, 143.

Bergeon, A., Mollaret, R., Henry, D., 2003. Soret effect and slow mass diffusion as a catalyst for overstability in Marangoni flows. Heat Mass Transfer 40, 105.

Bergeon, A., Burke, J., Knobloch, E., Mercader, I., 2008. Eckhaus instability and homoclinic snaking. Preprint.
Blanchflower, S., 1999. Magnetohydrodynamic convectons. Phys. Lett. A 261, 74.
Burke, J., Knobloch, E., 2006. Localized states in the generalized Swift–Hohenberg equation. Phys. Rev. E 73, 056211.
Castillo, J.L., Velarde, M.G., 1978. Thermal diffusion and the Marangoni instability of a two component fluid layer heated from below. Phys. Lett. A 66, 489.
Castillo, J.L., Velarde, M.G., 1982. Buoyancy-thermocapillary instability: the role of interfacial deformation in one- and two-component fluid layers heated from below or above. J. Fluid Mech. 125, 463.
Champneys, A.R., 1998. Homoclinic orbits in reversible systems and their applications in mechanics, fluids and optics. Physica D 112, 158.
Clerc, M.G., Falcon, C., Tirapegui, E., 2005. Additive noise induces front propagation. Phys. Rev. Lett. 94, 148302.
Deville, M., Fischer, P.F., Mund, E.H., 2002. High-order Methods for Incompressible Fluid Flow. Cambridge University Press, Cambridge.
Funaro, D., 1991. Polynomial Approximation of Differential Equations. Springer, New York.
Karniadakis, G.E., Israeli, M., Orszag, S.A., 1991. High-order splitting method for the incompressible Navier–Stokes equations. J. Comput. Phys. 97, 414.
Kolodner, P., 1993. Coexisting traveling waves and steady rolls in binary-fluid convection. Phys. Rev. E 48, R665.
Kolodner, P., Slimani, S., Aubry, N., Lima, R., 1995. Characterization of dispersive chaos and related states of binary-fluid convection. Physica D 85, 165.
Kozyreff, G., Chapman, S.J., 2006. Asymptotics of large bound states of localized structures. Phys. Rev. Lett. 97, 044502.
Mamun, C.K., Tuckerman, L.S., 1995. Asymmetry and Hopf bifurcation in spherical Couette flow. Phys. Fluids 7, 80.
Moore, D.R., Weiss, N.O., 2000. Resonant interactions in thermosolutal convection. Proc. R. Soc. London Ser. A 456, 39.
Prat, J., Mercader, I., Knobloch, E., 1998. Resonant mode interactions in Rayleigh–Bénard convection. Phys. Rev. E 58, 3145.
Sakaguchi, H., Brand, H.R., 1996. Stable localized solutions of arbitrary length for the quintic Swift–Hohenberg equation. Physica D 97, 274.
Sastry, S., Hijab, O., 1981. Bifurcation in the presence of small noise. Syst. Control Lett. 1, 159.
Tuckerman, L.S., 1989. Steady-state solving via Stokes preconditioning: recursion relations for elliptic operators. In: Dwoyer, D.L., Hussaini, M.Y., Voigt, R.G. (Eds.), Proceedings of the Eleventh International Conference on Numerical Methods in Fluid Dynamics, Springer, New York, p. 573.
Yochelis, A., Burke, J., Knobloch, E., 2006. Spatially localized oscillating states in periodically forced dissipative systems. Phys. Rev. Lett. 97, 254501.